

Constraints on Circumnuclear Disk through Free-Free Absorption in the Nucleus of 3C 84 with KaVA and KVN at 43 and 86 GHz

KIYOAKI WAJIMA,¹ MOTOKI KINO,^{2,3} AND NOZOMU KAWAKATU⁴

¹*Korea Astronomy and Space Science Institute, 776 Daedeokdae-ro, Yuseong, Daejeon 34055, Korea*

²*Kogakuin University of Technology & Engineering, Academic Support Center, 2665-1 Nakano, Hachioji, Tokyo 192-0015, Japan*

³*National Astronomical Observatory of Japan, 2-21-1 Osawa, Mitaka, Tokyo 181-8588, Japan*

⁴*National Institute of Technology, Kure College, 2-2-11 Agaminami, Kure, Hiroshima 737-8506, Japan*

(Received; Revised; Accepted)

Submitted to ApJ

ABSTRACT

The nearby bright radio galaxy 3C 84 at the center of Perseus cluster is one of the ideal targets to explore the jet in active galactic nuclei (AGNs) and its parsec-scale environment. A recent research of Fujita & Nagai revealed the existence of the northern counter-jet component (N1) located at ~ 2 mas north from the central core in VLBI images at 15 and 43 GHz and they are explained by the free-free absorption (FFA) due to an ionized plasma foreground. Here we report a new quasi-simultaneous observation of 3C 84 with the Korean VLBI Network (KVN) at 86 GHz and the KVN and VERA (VLBI Exploration of Radio Astrometry) Array (KaVA) at 43 GHz in 2016 February. We succeeded the first detection of N1 at 86 GHz and the data show that N1 still has an inverted spectrum between 43 and 86 GHz with its spectral index α ($S_\nu \propto \nu^\alpha$) of 1.19 ± 0.43 , while the approaching lobe component has the steep spectrum with the index of -0.54 ± 0.30 . Based on the measured flux asymmetry between the counter and approaching lobes, we constrain the averaged number density of the FFA foreground n_e as $1.8 \times 10^4 \text{ cm}^{-3} \lesssim n_e \lesssim 1.0 \times 10^6 \text{ cm}^{-3}$. Those results suggest that the observational properties of the FFA foreground can be explained by the dense ionized gas in the circumnuclear disk and/or assembly of clumpy clouds at the central ~ 1 pc region of 3C 84.

Keywords: galaxies: active — galaxies: individual (3C 84) — radio continuum: galaxies — techniques: interferometric

1. INTRODUCTION

Active galactic nuclei (AGNs) is widely believed to have an obscuring structure near a central supermassive black hole (SMBH), which is described in the AGN unified model (e.g., Antonucci 1993; Urry & Padovani 1995). Indeed, there is mounting evidence that it has a rich structure within 10 pc scale from the recent progresses of spatially resolved multi-wavelength observations. At near- to mid-infrared (NIR to MIR) wavelengths thermal dust emission in AGNs support the existence of compact obscuring structures within 10 pc of the central engine (e.g., Jaffe et al. 2004; Burtcher et al. 2013; Asmus et al. 2014). Recent ALMA observations revealed that multi-phase dynamic nature in the circumnuclear disk (CND) region of larger than 10 pc, i.e., the diffuse

atomic gas is more spatially extended along the vertical direction of the disk than the dense molecular gas (Izumi et al. 2018). Due to energy feedback from AGNs and nuclear starburst, co-existence of ionized gas and cold gas is expected on the CND scale (e.g., Wada et al. 2016). Dense molecular gas disks with their sizes of 10 pc, which may be an outer part of a few parsec obscuring structure, have been found around nearby Seyfert nuclei (e.g., Hicks et al. 2013; Davies et al. 2014; Imanishi et al. 2016, 2018; Izumi et al. 2018). Such a CND would be a massive reservoir of molecular gas, which potentially triggers an active star formation. A prominent star formation has been found as a nuclear starburst (e.g., Imanishi & Wada 2004; Davies et al. 2007; Imanishi et al. 2011; Diamond-Stanic & Rieke 2012; Alonso-Herrero et al. 2014; Esquej et al. 2014; Mallmann et al. 2018), which may be related to the CND structure (Kawakatu & Wada 2008; Kawakatu et al. 2020).

Despite the above-shown progresses on the scale of larger than a few pc, it is not yet clear about the physical properties of the obscuring structure on the scale of smaller than 1 pc. There are a number of theoretical models arguing possible origins, e.g., (1) radiation pressure from AGN (e.g., Krolik 2007; Namekata et al. 2014; Namekata & Umemura 2016), (2) radiation pressure from nuclear starburst (e.g., Thompson et al. 2005), (3) high velocity dispersion clouds/clumps model (Krolik & Begelman 1988; Vollmer et al. 2008), (4) turbulent pressure from type II supernova explosions (Wada & Norman 2002; Wada et al. 2009), (5) disk winds (e.g., Elitzur & Shlosman 2006; Nomura et al. 2016), (6) outflows driven by AGN radiation pressure (Wada 2012; Wada et al. 2016; Dorodnitsyn et al. 2016; Chan & Krolik 2016, 2017), and (7) chaotic cold accretion (CCA) within the inner kpc (Gaspari et al. 2013). In order to investigate its physical origin in details on < 1 pc scale, high-resolution observations of the hot ionized gas around AGNs are essential to understand basic properties of multi-phase CNDs. As previous researchers have been carried out mainly with very long baseline interferometer (VLBI) at centimeter wavelengths (e.g., Kamenon et al. 2000, 2001), the free-free absorption is one of useful tools to explore the ionized gas around AGNs.

The compact radio source 3C 84 (also known as NGC 1275) is one of the nearby ($z=0.018$) best-studied radio galaxies. Proximity of the object allows us to make detailed observations about the environment around the SMBH on 1 pc scale. Abdo et al. (2009) reported increase in the radio flux at 14.5 GHz starting in 2005 with long-term monitoring by the the University of Michigan Radio Astronomy Observatory. They claimed that this radio flare could be interpreted as an ejection of new jet components. This was confirmed by Nagai et al. (2010), who found the emergence of a newborn bright component, designated as C3, with multi-epoch VLBI monitoring during 2006 – 2009. C3 showed a proper motion toward the southern direction with an apparent velocity of $0.2 - 0.3c$ (Nagai et al. 2010; Suzuki et al. 2012; Hiura et al. 2018). Walker et al. (2000) conducted multi-epoch, multi-frequency VLBA (Very Long Baseline Array) observations of 3C 84 with the frequency range of 0.3 to 43.2 GHz, resulting in detection of free-free absorbed emission in the northern lobe located at ~ 8 mas from the core. They suggested that the absorption feature is due to the existence of 3 pc-scale absorber.

Fujita & Nagai (2017) firstly reported the existence of the northern counter-jet component, designated as N1, in 3C 84 at both 15 and 43 GHz with VLBA. This feature is considered to be a counter jet component corresponding to the approaching jet located at the south. N1 has a strongly inverted spectrum, which indicates that it is absorbed by an ionized plasma around the SMBH via FFA. So far, however, no detection of

N1 has been made at higher frequency than 43 GHz. Observations at 86 GHz or even higher frequencies offer a unique view on the environment of the radio jet in 3C 84 since the radio emission would be more transparent at such frequencies.

In this paper we report the results of VLBI observation of 3C 84 at 86 GHz, which focuses on properties of newly detected northern component, together with the quasi-simultaneous 43 GHz image obtained in our previous work summarized in Kino et al. (2018). By combining the northern counter lobe images at 86 and 43 GHz, we show the spectral index between these frequencies and also discuss properties and geometry of sub-pc-scale structure and the circum-nuclear environment in 3C 84.

Throughout this paper, we define the spectral index, α , as $S_\nu \propto \nu^\alpha$, where S_ν is the flux density at the frequency ν , and we adopt a Λ CDM cosmology with $H_0 = 71 \text{ km s}^{-1} \text{ Mpc}^{-1}$, $\Omega_\Lambda = 0.73$, and $\Omega_M = 0.27$ (Komatsu et al. 2009), corresponding to an angular-to-linear scale conversion of 0.36 pc mas^{-1} for 3C 84.

2. OBSERVATIONS AND DATA REDUCTION

Our observations were conducted with the KVN (Korean VLBI Network) and VERA (VLBI Exploration of Radio Astrometry) array (hereafter KaVA) on 2016 February 22 at 43.2 GHz with the total on-source time of 475 minutes, and with KVN on 2016 February 23 at 86.2 GHz with the total on-source time of 737 minutes. The KaVA 7-telescope data was correlated using the Daejeon Hardware Correlator (Lee et al. 2015a) with the output preaveraging time of 1.6 seconds, whereas the DiFX correlator (Deller et al. 2011) was used for the KVN 3-telescope data correlation with the output pre-averaging time of 2 seconds.

The data were reduced using the Astronomical Image Processing System (AIPS) software (Greisen 2003) for amplitude and phase calibration, and the Caltech software Difmap (Shepherd 1997) for imaging and self-calibration. We applied *a priori* amplitude calibration using the antenna gain factors and system noise temperature measurements with the AIPS task APCAL. We also applied the amplitude correction factor with APCAL, as mentioned by Lee et al. (2015b). Bandpass calibration for both amplitude and phase is employed with the AIPS task BPASS. Fringe fitting was done using the AIPS task FRING with the solution interval of 30 seconds, resulting in successful fringe detection on all baselines for whole observing time. Fringe-fitted data were exported to Difmap for imaging. We applied the amplitude and phase self-calibration to KaVA's data and could reconstruct the source model using the visibility for all baselines with the maximum error of 6%. Although we could not apply the amplitude self-calibration to KVN's data because of small number of antennas, we believe that the visibility amplitude

of KVN’s data was calibrated well since dense measurement (every 10 seconds) of the system noise temperature was made at all KVN stations. To estimate the amplitude calibration error of KVN’s data, we compared the observation results of a bright quasar 3C 273 obtained by the KVN key science program, iMOGABA (interferometric monitoring of gamma-ray bright AGNs; Lee et al. 2016), and a VLBA observation, both of which were conducted quasi-simultaneously (2014 February 28 and 26 for iMOGABA and VLBA, respectively) at 86 GHz by employing the same amplitude calibration procedure as that of our observation of 3C 84. As a result, we confirmed that the peak intensity and total CLEANed flux of each observation are coincident within the range of 15%. To ensure a better sensitivity, we adopted natural weighting of the data with gridding weights scaled by amplitude errors raised to the power of -1 . Details of the image dynamic range (DR) obtained with KaVA at 43 GHz have been reported by Kino et al. (2018), while DR of 100 was obtained for the image at 86 GHz with KVN.

3. RESULTS

Figure 1 shows images of 3C 84 with KaVA at 43 GHz and KVN at 86 GHz. Restored KaVA image with the synthesized beam of the KVN 86 GHz image is also shown in Figure 1. The source consists of two bright components, the central core component (hereafter C1) and the southern lobe component (hereafter C3), both of which were identified in the previous VLBI observations (e.g., Nagai et al. 2010, 2012, 2014). On the other hand, we could identify N1 in the north of C1 with the separation angle of 2.5 mas. This is already reported by Fujita & Nagai (2017) as mentioned in Section 1, whereas we could identify N1 at 86 GHz as well as 43 GHz. The detection level of N1 is about 6 times the off-source rms noise ($\sigma = 13$ mJy and 65 mJy at 43 and 86 GHz, respectively) at both frequencies.

Figure 2 shows the spectral index map of 3C 84 between KaVA at 43.2 GHz and KVN at 86.2 GHz. Both observations do not employ the phase-referencing technique, resulting in the loss of the absolute position through the self-calibration procedure (Pearson & Readhead 1984; Thompson et al. 2001). We therefore superposed two images with reference to C3 since it shows an optically thin feature at the peak intensity position. To confirm this feature quantitatively, we estimate α of each component. Table 1 shows peak intensities of each component at 43.2 and 86.2 GHz, corresponding to the center and right panels in Figure 1, and α between these frequencies. C1 and C3 show its spectral index of -0.11 ± 0.35 and -0.54 ± 0.30 , respectively, suggesting that C1 is the self-absorbed core and C3 is the optically thin component, whereas N1 has an optically thick spectral feature with α of $+1.19 \pm 0.43$ (see also Figure 2). Although optically thick spectral feature can also be seen in the north-

Table 1. Peak intensity and spectral index of each component.

Component	I_{peak} [Jy beam $^{-1}$]		α_{43}^{86}
	43.2 GHz	86.2 GHz	
C1	6.28 ± 0.02	5.82 ± 0.08	-0.11 ± 0.35
C3	6.82 ± 0.02	4.71 ± 0.08	-0.54 ± 0.30
N1	0.18 ± 0.02	0.41 ± 0.08	$+1.19 \pm 0.43$

NOTE—Column 1: component name; Columns 2 and 3: peak intensity of a restored image at 43.2 GHz with KaVA with the restored beam size of $1.36 \text{ mas} \times 0.78 \text{ mas}$ and the position angle of the major axis of $82.^\circ 3$, and at 86.2 GHz with KVN; Column 4: spectral index.

east of C1, we believe that this is not a real one because of lower signal-to-noise ratio in the images at both frequencies at around this area compared to that in the central region of the component. To check fidelity of the spectral index map, we examined an effect of registration error between images at each frequency taking into account the expected amplitude error of the peak intensity of 15% shown in Section 2. If we assume that the 15% difference of the peak intensity comes from the positional difference of the Gaussian component, possible registration error of C3 becomes ± 0.32 mas in the right ascension and ± 0.19 mas in the declination. Assuming the maximum registration error between each image shown above, resultant spectral index maps between 43 and 86 GHz show that α at the peak position of N1 is inverted for all cases although an optically thick region always appears at the edge of C1, probably due to lower signal-to-noise ratio. We thus do not discuss a physical property at the edge of C1 in this paper.

The measured α for both C1 and C3 is consistent with previous results by Suzuki et al. (2012), in which C1 is the radio core and C3 is the hot spot component (i.e., a termination shock). Comparison of α between C1 and N1 clearly indicates that N1 suffers strong absorption from the intervening FFA foreground, which has been already claimed by Fujita & Nagai (2017).

4. DISCUSSION

In this section, we discuss physical properties of the FFA foreground which exists somewhere along our line of sight to N1. The pioneering work of Walker et al. (2000) showed that synchrotron emission from the northern counter radio lobe located at the 5 – 10 mas from C1 is obscured by a FFA foreground for the first time. In the present work, we investigate the newly emerged northern counter-jet component N1 located around 2 mas from C1. Using the observational prop-

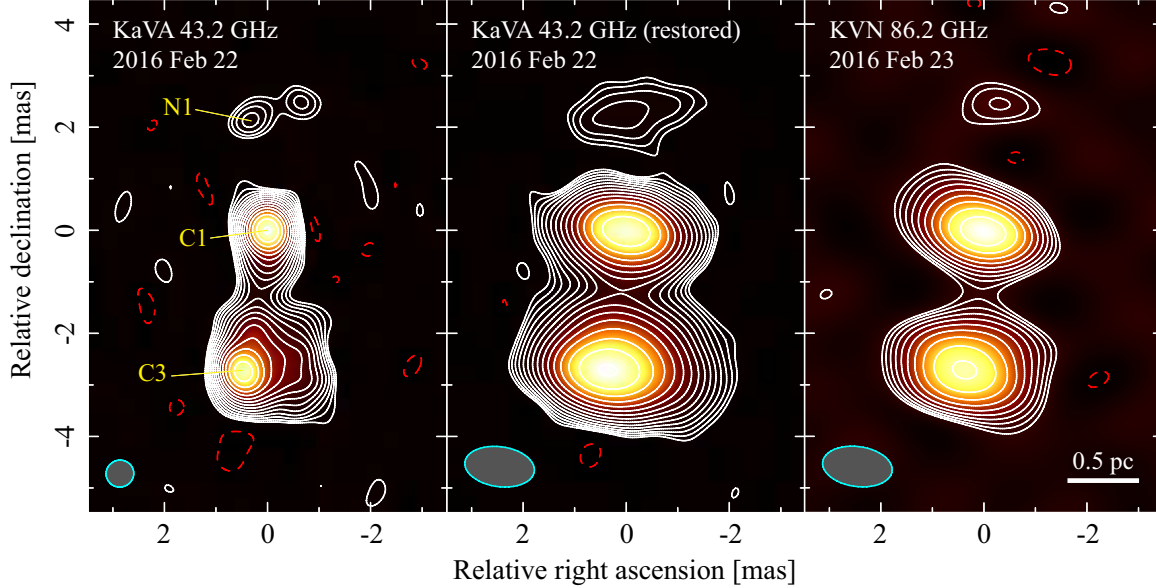


Figure 1. VLBI images of 3C 84 obtained by KaVA and KVN. (Left) KaVA image of 3C 84 on 2016 February 22 at 43.2 GHz. (Center) Same as the left panel but the synthesized beam is restored with the same size as that of the right panel. (Right) KVN image of 3C 84 on 2016 February 23 at 86.2 GHz. In all figures the lowest contour is three times the off-source rms noise (σ). The dashed and solid curves show negative and positive contours, respectively, and the contour levels are -3σ , $3\sigma \times (\sqrt{2})^n$ ($n = 0, 1, 2, \dots$). The restoring beam with its size of $0.54 \text{ mas} \times 0.52 \text{ mas}$ at a position angle of -72° (left) or $1.36 \text{ mas} \times 0.78 \text{ mas}$ at a position angle of 82° (center and right) is indicated in the lower left corner of each image.

erties of N1, here we investigate physical properties of the FFA foreground. While Walker et al. (2000) discussed only a geometrically thin disk as the FFA foreground, we argue both of a geometrically thin circumnuclear disk and assembly of clumpy clouds as the FFA foreground in light of current understanding of more realistic picture of AGN nucleus structure (Wada 2012; Wada et al. 2016; Izumi et al. 2018). The considered structure is summarized in a schematic picture shown in Figure 3. Hereafter we assume that the plasma composition of the FFA foreground is a pure hydrogen. Hence, an electron number density equals to that of protons.

4.1. FFA Opacity

First, we estimate the FFA opacity for foreground seen at 86 GHz and 43 GHz. It is well known that the theoretically known FFA opacity for the case of uniformly distributed plasma is given by

$$\tau_{\text{ff}}(\nu) \approx 25 \left(\frac{L}{1 \text{ pc}} \right) \left(\frac{n_e}{10^4 \text{ cm}^{-3}} \right)^2 \left(\frac{T_e}{10^4 \text{ K}} \right)^{-1.5} \left(\frac{\nu}{1 \text{ GHz}} \right)^{-2}, \quad (1)$$

where T_e and n_e are the temperature and the electron density of absorbing matter, respectively, and L is the path length along the line of sight (Levinson et al. 1995). Correspondingly, a change in the FFA depth, $\delta\tau_{\text{ff}}$, for a given frequency can be expressed as

$$\delta\tau_{\text{ff}} = \left(\frac{\delta L}{L} + 2 \frac{\delta n_e}{n_e} - 1.5 \frac{\delta T_e}{T_e} \right) \tau_{\text{ff}}. \quad (2)$$

From this, one can discuss which quantity mainly contributes to the $\delta\tau_{\text{ff}}$ in different epochs.

Assuming that C3 and the corresponding counter-lobe component N1 have intrinsically same intensities (Fujita & Nagai 2017), one can obtain τ_{ff} as

$$\exp[-\tau_{\text{ff}}(\nu)] = \frac{I_{\text{N1}}}{I_{\text{C3}}}, \quad (3)$$

where I_{C3} and I_{N1} are the peak intensity of C3 and N1, respectively. Using Equation (3) and the measured I_{N1} and I_{C3} , we obtain $\tau_{\text{ff}} = 2.4 \pm 0.2$ at 86 GHz and 3.6 ± 0.1 at 43 GHz, respectively. The ratio of τ_{ff} between 43 and 86 GHz, which is given by $\gamma = \log[\tau_{\text{ff}}(86\text{GHz})/\tau_{\text{ff}}(43\text{GHz})]/\log 2 = -0.57 \pm 0.10$ is significantly different from $\gamma = -2$ which indicates a non-uniformity of FFA even if the error of γ is taken into account. Note that this well agrees to that derived between 15 and 43 GHz (Fujita & Nagai 2017). We also note that the spectral index map between the subsequent two frequencies does not provide the turn-over frequency of FFA. For its determination, VLBI observations at higher frequencies would be needed.

4.2. Physical Properties of FFA Foreground

As mentioned in Section 4.1, our observational results suggest the existence of an optically thick, ionized non-uniform plasma foreground, which may be an inner part of the rotational disk of the molecular gas within $\sim 100 \text{ pc}$ detected by ALMA (Nagai et al. 2019), although our estimation of γ cannot constrain an exact location of the FFA foreground. As

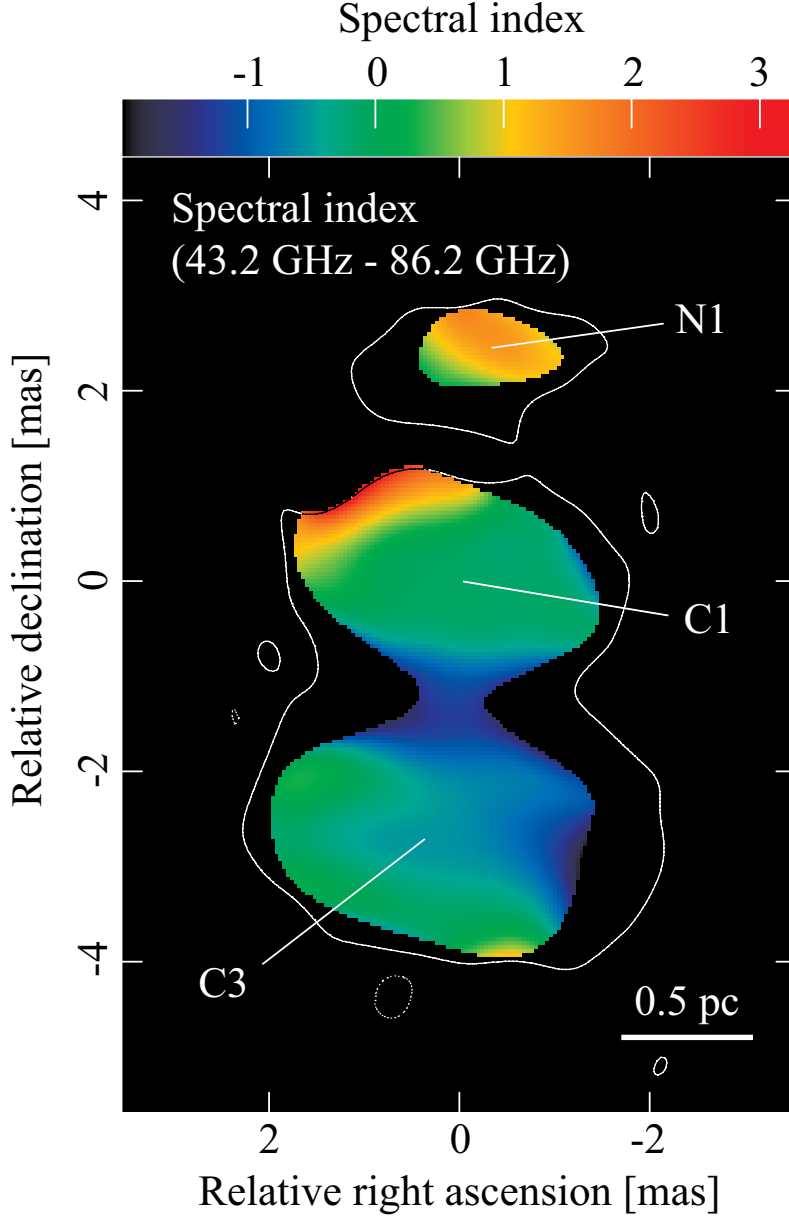


Figure 2. Spectral index map of 3C 84 derived from the flux densities at 43.2 GHz with KaVA on 2016 February 22 and 86.2 GHz with KVN on 2016 February 23. The top color bar indicates the spectral index α ($S_\nu \propto \nu^\alpha$). The map corresponds to an area greater than 3σ noise level of the KVN image at 86.2 GHz, and the solid lines show the lowest contour corresponding to the 3σ image noise of the restored KaVA image at 43.2 GHz.

for the origin of FFA foreground, there are two possible cases to be realized. One is (1) a CND in which the plasma density changes in the radial direction with its size of 10 pc (see Figure 3). Another one is (2) an assembly of clumpy clouds, which are the main structure of AGNs such as the broad-line region, narrow-line region, clumpy torus and polar dust (Figure 1 in Ramos Almeida & Ricci 2017). Below we discuss physical properties of CNDs and clumps in Sections 4.2.1 and 4.2.2, respectively.

4.2.1. Properties of CNDs

First, we discuss the case in which a circumnuclear disk with a constant half-opening angle (ϕ_{disk}) is responsible for FFA (see Figure 3). The CND has a radial profile in n_e . The path length (L) and its change (δL) depend on the distance between N1 and C1, l_N and the inclination angle of CND, θ . These are given by

$$L = \frac{\sin\theta \sin 2\phi}{\cos(\theta + \phi) + \cos(\theta - \phi)} l_N, \quad \frac{\delta L}{L} = \frac{\delta l_N}{l_N} \lesssim 0.4. \quad (4)$$

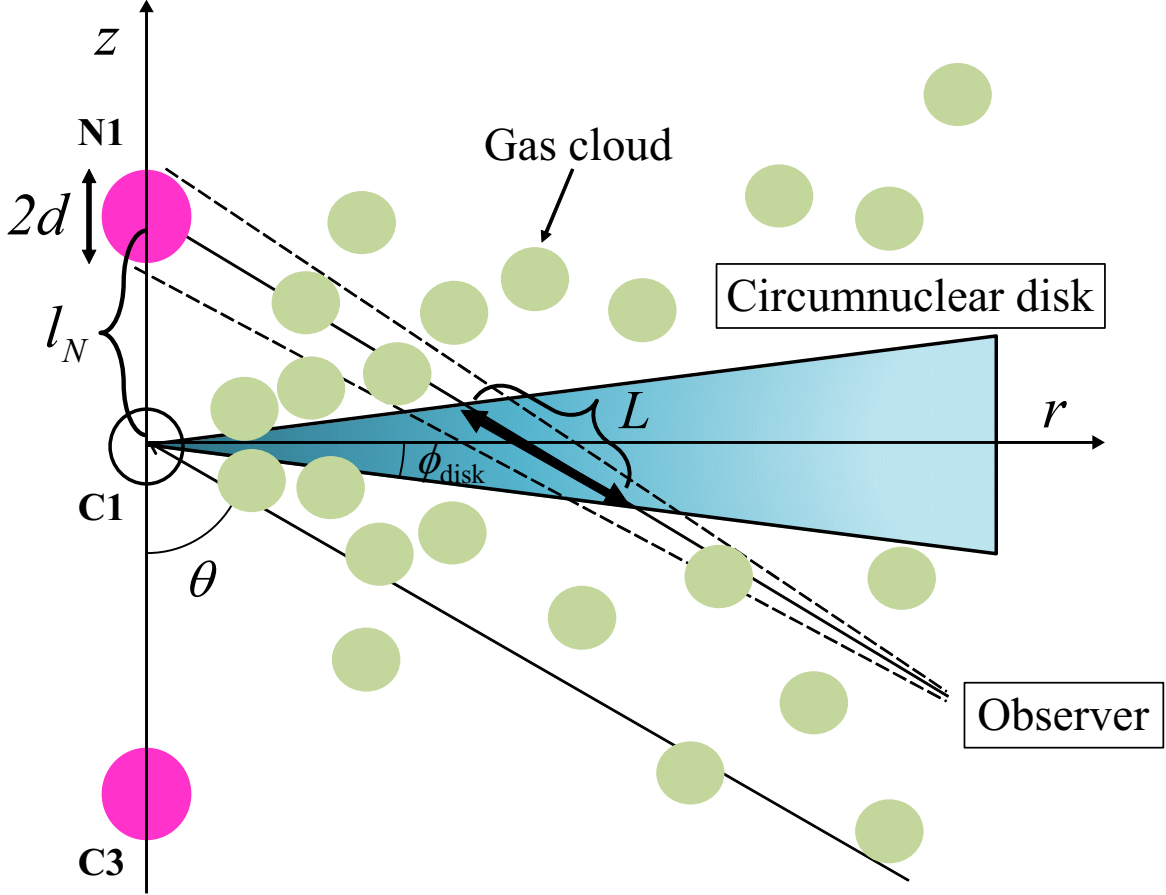


Figure 3. A simple model of free-free absorption circumnuclear disk in which the plasma density gradually changes in the radial direction. The path length L depends on l_N (apparent distance between C1 and N1), θ (jet viewing angle), and ϕ_{disk} (half-opening angle of the disk). The clumpy clouds with high velocity dispersion are located above the circumnuclear disk.

Therefore, the change of the geometric path length is not likely a main contributor in $\delta\tau_{\text{ff}}$ (see Equation 2) within our observational period. It is known that $l_N = 2.2(\sin\theta)^{-1}$ pc and the range of θ is constrained as $18^\circ < \theta < 65^\circ$ by Tavecchio & Ghisellini (2014) and Fujita & Nagai (2017). Here, the minimum half opening angle is assumed as $\phi_{\text{disk}} = 0.5$ (i.e., scale height $h \simeq 0.01r$, where r is a radial distance from C1) based on a hydrostatic ionized disk structure (see Section 3 in Levinson et al. 1995). Such a geometrically thin disk is observationally indicated from the large value of the rotation measurement at 230 GHz (Plambeck et al. 2014). As for maximum ϕ_{disk} , we set the condition of $\phi_{\text{disk}} < 90^\circ - \theta$, since the radio emission from C1 is not absorbed by the foreground CND (see Figure 2; Plambeck et al. 2014; Kim et al. 2019). Then, we obtain the corresponding allowed range of L in Table 2, i.e., $0.04 \text{ pc} \lesssim L \lesssim 23 \text{ pc}$. The allowed path length is fairly wide due to the wide range of the allowed θ . For instance, the lower limit of $L \approx 0.04 \text{ pc}$ realizes with the narrowest viewing angle of $\theta = 18^\circ$. This lower limit of $L \approx 0.04 \text{ pc}$ would correspond to the geometrical thickness of the innermost part of CND.

Table 2. Path length L for various models.

$\phi_{\text{disk}} [^\circ]$	L [pc]		
	$\theta = 18^\circ$	$\theta = 40^\circ$	$\theta = 65^\circ$
0.5	0.042	0.065	0.22
5	0.43	0.66	2.23
10	0.86	1.35	5.07
15	1.31	2.12	9.85
20	1.80	3.01	22.9
25	2.32	4.13	*
30	2.91	5.66	*
35	3.59	8.02	*
40	4.41	12.5	*
45	5.44	*	*
50	6.82	*	*
60	12.3	*	*

NOTE—*: C1 is hidden by CNDs.

In Figure 4, we show the n_e of the CND, which satisfies $\tau_{\text{ff}} = 1$ for given L and T_e . Hereafter we do not treat the vertical structure of the disk but just discuss an averaged number density (n_{CND}) along the given L . The derived number density resides in

$$1.8 \times 10^4 \text{ cm}^{-3} \lesssim n_{\text{CND}} \lesssim 1.0 \times 10^6 \text{ cm}^{-3}, \quad (5)$$

properly taking possible uncertainties of the CND's L and T_e into account. Regarding T_e , the ionization condition requires the lower limit of T_e as $T_e \approx 1 \times 10^4$ K. The upper limit of T_e is governed by atomic line cooling in the FFA foreground (Levinson et al. 1995). Since the line cooling function is peaked around $T_e \approx 1 \times 10^4$ K (Sutherland & Dopita 1993), the assumed upper limit of T_e should not be significantly different from $T_e \approx 1 \times 10^4$ K. Following Levinson et al. (1995), we set the upper limit as $T_e \approx 3 \times 10^4$ K in this work.

The column density, N_{H} , is more convenient quantity than n_{CND} for comparison of the obtained n_{CND} with numerical simulations and other observations. In Figure 4, we overlay several lines with its N_{H} being constant, as given by

$$N_{\text{H}} \approx 3 \times 10^{23} \text{ cm}^{-2} \left(\frac{n_{\text{CND}}}{10^5 \text{ cm}^{-3}} \right) \left(\frac{L}{1 \text{ pc}} \right). \quad (6)$$

Wada et al. (2016) examined the structure and dynamics of molecular, atomic, and ionized gases around an AGN by using three-dimensional radiation-hydrodynamic simulations. They found that inhomogeneous ionized gas are a geometrically thick, while dense molecular gases are distributed near the equatorial plane. If the viewing angle for the nucleus is larger, e.g., $\theta \geq 50^\circ$, the column density is consistent with our observation. Thus, our observation might trace the parts of ionized gas demonstrated by radiation-hydrodynamic simulations. It is also interesting to note that Hitomi Collaboration et al. (2018) reported the detection of the Fe-K α fluorescence line at 6.4 keV from 3C 84 with the Soft X-ray Spectrometer on board the Hitomi satellite with its equivalent width of ~ 20 eV. They derived N_{H} as $N_{\text{H}} f_{\text{cov}} \sim 3.0 \times 10^{22} \text{ cm}^{-2}$, where f_{cov} is the covering fraction of the fluorescing material, from the Hitomi observation. They discuss a possible matter distribution in case of the fluorescing material being located at a distance of 100 pc from the central engine. A small f_{cov} (~ 0.02) can be derived if their result accommodates to the electron density of the [Fe II] emitters ($\sim 4000 \text{ cm}^{-3}$) obtained with the NIR observation by Gemini (Scharwächter et al. 2013). When adopting this $f_{\text{cov}} \sim 0.02$, N_{H} becomes $\sim 1 \times 10^{24} \text{ cm}^{-2}$, which is comparable to our results with L of a few pc and n_e of a few $\times 10^5 \text{ cm}^{-3}$ shown in Figure 4. It may indicate a possibility that the Hitomi satellite detected the fluorescence line from a few pc region of CNDs that absorbed the synchrotron emission from N1.

It is important to verify that the picture described above is consistent with the non-detection of N1 in the last decade.

Since $\delta L/L$ is too small to change $\delta \tau_{\text{ff}}$ in our observational period, $\delta n_{\text{CND}}/n_{\text{CND}}$ would be a main contributor of $\delta \tau_{\text{ff}}$. It is expected that n_{CND} is larger in earlier observational epochs. As an example, we reanalyzed one epoch of VLBA archive data at 43 GHz conducted on 2012 October 29, which showed non-detection of N1 (Jorstad et al. 2017). The data shows the peak intensity of the southern component of $1.94 \text{ Jy beam}^{-1}$ with the $1-\sigma$ image noise of $4.2 \text{ mJy beam}^{-1}$. If we set the detection criterion of N1 as 5 times the image noise, the upper limit of the peak intensity of N1 shall become 21 mJy beam^{-1} , resulting in the lower limit of the opacity to be 4.5. Assuming the typical values of T_e of 1×10^4 K and $L = 0.5 \text{ pc}$ for 2012 October, $n_{\text{CND}} \gtrsim 2.6 \times 10^5 \text{ cm}^{-3}$ is required to accommodate the opacity obtained by VLBA to the result of non-detection of N1. On the other hand, taking the same typical values of $L \approx 0.5 \text{ pc}$ and $T_e \approx 1 \times 10^4$ K and applying $\tau_{\text{ff}} = 3.6$ which was taken by our KaVA observation in 2016, we obtain $n_{\text{CND}} \approx 2.3 \times 10^5 \text{ cm}^{-3}$, which is smaller than n_{CND} in 2012. Although the change is too subtle to draw a conclusion, the comparison of two-epoch images obtained in 2012 and 2016 indicates a slightly larger n_{CND} for earlier epoch, which is consistent with a radial gradient in the disk. To make a clear conclusion, further yearly timescale long term monitoring of 3C 84 is much awaited.

4.2.2. Properties of Clumpy Gas Clouds

Second, we discuss the case in which clumpy gas clouds are responsible for FFA (the clouds in Figure 3). This idea is motivated by recent observations of 10 pc obscuring structures in nearby AGNs with ALMA (García-Burillo et al. 2014; Imanishi et al. 2016, 2018; Izumi et al. 2018). The detailed obscuring structures revealed by ALMA consist of not only a dusty disk, but also clumpy gas clouds with high velocity dispersion implied by supernovae and/or AGN radiative feedbacks (e.g., Wada et al. 2016; Izumi et al. 2018; Kawakatu et al. 2020). Hence, we consider the case in which clumpy gas clouds dominantly absorb the synchrotron radio emission from N1. In the clouds-dominated case, the FFA optical depth can be written as

$$\begin{aligned} \tau_{\text{ff}} &= \bar{\tau}_{\text{ff}} N_c \\ &\approx 25 \left(\frac{N_c}{10} \right) \left(\frac{r_c}{0.1 \text{ pc}} \right) \left(\frac{\bar{n}_c}{10^4 \text{ cm}^{-3}} \right)^2 \left(\frac{T_e}{10^4 \text{ K}} \right)^{-1.5} \left(\frac{\nu}{1 \text{ GHz}} \right)^{-2} \end{aligned} \quad (7)$$

where $\bar{\tau}_{\text{ff}}$, N_c , r_c and \bar{n}_c are the average FFA optical depth of each cloud, the total number of clouds in the line of sight and the size of a cloud, and the number density of each cloud, respectively. Here, we note that $\bar{\tau} = \alpha_{\text{ff}} r_c$ where α_{ff} is the free-free absorption coefficient.

Assuming N_c is comparable to the mean number of clouds along radial equatorial ray for Seyfert galaxies derived by the IR SED fitting (e.g., Alonso-Herrero et al. 2011; Ramos Almeida et al. 2011; Ichikawa et al. 2015;

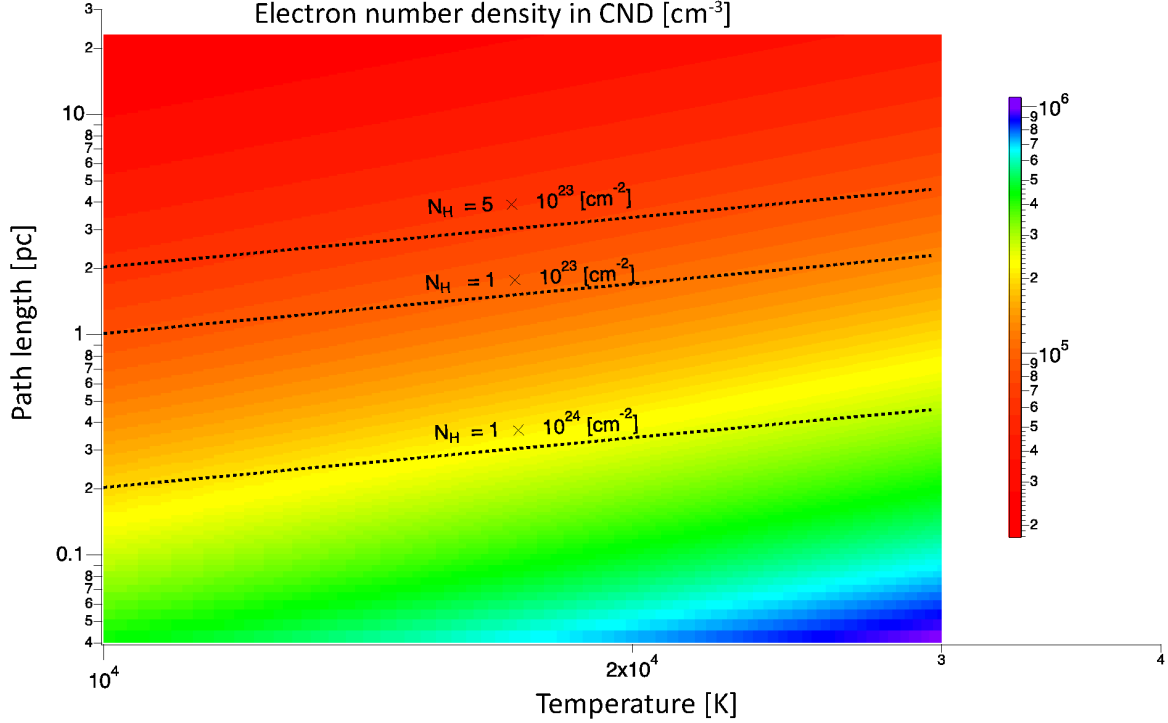


Figure 4. Estimated electron number density (n_{CND}) in case of the circumnuclear disk (CND) being the FFA foreground. The color bar represents the estimated n_{CND} for given T_e and L , and the value is in the range of $1.8 \times 10^4 \text{ cm}^{-3} \lesssim n_{\text{CND}} \lesssim 1.0 \times 10^6 \text{ cm}^{-3}$. The three dashed lines indicate the cases corresponding to the constant column density, N_{H} , of $1 \times 10^{23} \text{ cm}^{-2}$, $5 \times 10^{23} \text{ cm}^{-2}$, and $1 \times 10^{24} \text{ cm}^{-2}$.

Audibert et al. 2017), i.e., $N_c \simeq 3-15$, we find that $\bar{\tau}_{\text{ff}}$ at 86 GHz becomes $\simeq 0.2-1.2$, which is of the order of unity and agrees with observational properties of N1.

To constrain the number density of the clump, getting the size of the clump (r_c) should be required. The size of self-gravitating clump in the context of AGNs have been estimated in literatures (e.g., Krolik & Begelman 1988; Hönig & Beckert 2007; Kawaguchi & Mori 2011). According to them, we have $r_c \leq 0.05 \text{ pc}$ at 1 pc from the central SMBH with $M_{\text{BH}} = 8 \times 10^8 M_{\odot}$ (Scharwächter et al. 2013). On the other hand, the size of clumps can be constrained by the observations of transient X-ray absorption events in nearby AGNs, i.e., the typical size is 0.002 pc (e.g., Markowitz et al. 2014; Tanimoto et al. 2019). By adopting N_c and r_c taking into account their uncertainties of $3 \leq N_c \leq 15$ and $0.02 \text{ pc} \leq r_c \leq 0.05 \text{ pc}$, the lower limit of number density of each ionized cloud \bar{n}_c can be given by

$$3 \times 10^5 \text{ cm}^{-3} \leq \bar{n}_c \leq 4 \times 10^6 \text{ cm}^{-3}. \quad (8)$$

In case of ionized gas clumps, the typical Thomson scattering opacity of each cloud can be estimated as $\bar{\tau}_{\text{T}} \sim 1.5 \times 10^{-2}$ since the optical depth is given by $\tau_{\text{T}} = \sigma_{\text{T}} \bar{n}_c r_c$, where σ_{T} is the Thomson cross section. If we adopt the opacity ratio of the dusty gas and ionized gas is $\simeq 10^3$ at the UV band for the AGN radiation (e.g., Umemura et al. 1998; Ohsuga & Umemura 2001; Wada 2012), the optical depth of each cloud is $\bar{\tau}_{\text{UV}} = 10^3 \times \bar{\tau}_{\text{T}} \simeq 15$, which is consistent

with the lower value for nearby Seyfert galaxies (e.g., Table 10 in Ramos Almeida et al. 2011). This might indicate that the ionized gas is also clumpy within 1 pc region of 3C 84. Wada et al. (2018) examine properties of the ionized gas irradiated by less luminous AGN such as Seyfert galaxies based on their “radiation-driven fountain” model (Wada 2012). They found that the ionized region show non-uniform internal structures, corresponding to the clumpy fountain flows caused by the radiation pressure on dusty gas, although the typical density ($\bar{n}_c \simeq 10^3 \text{ cm}^{-3}$) is smaller than our estimate. In addition, by the optical/NIR observations, the existence of dense clumps with $\bar{n}_c \simeq 10^5 \text{ cm}^{-3}$ has been reported from the detection of coronal lines within NLR (e.g., Murayama & Taniguchi 1998). These high density clouds in NLRs might contribute the absorption feature of N1.

Alternatively, since the density is comparable to number density $n_c \simeq 10^{3-5} \text{ cm}^{-3}$, based on the momentum balance between the jet thrust and the ram pressure from the clump (Nagai et al. 2017; Kino et al. 2018), these ionized clumps may contribute not only the absorption of counter jet but also the feedback on jets. Since the dust sublimation radius of 3C 84 is $\sim 0.1 \text{ pc} (L_{\text{UV}}/10^{43} \text{ erg s}^{-1})^{0.5}$ (e.g., Kino et al. 2018), the dust components in these dense clumps could be survived. If this is the case, the clumpy clouds might be related to the polar elongation in MIR continuum emission distributions revealed by high-resolution observa-

tions in nearby Seyfert galaxies (e.g., [Tristram et al. 2014](#); [Asmus et al. 2016](#); [López-Gonzaga et al. 2016](#)).

Lastly, it is worth mentioning that the size of clumpy clouds may be constrained by the multi-epoch observation of FFA, which is left in our future work, since the typical timescale of flux variability may be related to the hot spots crossing time, i.e., $t_{\text{cross}} \sim r_c/v_h \simeq 2.5$ yr by assuming $r_c = 0.05$ pc and the head speed of jets $v_h \simeq 0.2c$ (e.g., [Nagai et al. 2010](#); [Suzuki et al. 2012](#); [Hiura et al. 2018](#)). If we detect the flux variability with a few years, it may clarify whether the clumpy clouds are main absorbers rather than the CNDs.

5. SUMMARY

By conducting quasi-simultaneous VLBI observations at 43 and 86 GHz with KaVA and KVN, we explore sub-parsec scale structure of a nearby bright radio galaxy 3C 84 via the optically thick FFA features. Here we summarize our main findings.

- We conducted a new quasi-simultaneous observation of 3C 84 with KVN at 86 GHz and KaVA at 43 GHz in 2016 February. We succeeded the first detection of N1 at 86 GHz and the data show that N1 still has an inverted spectrum between 43 and 86 GHz with its spectral index α ($S_\nu \propto \nu^\alpha$) of 1.19 ± 0.43 , while the approaching lobe component C3 has the steep spectrum with α of -0.54 ± 0.30 .
- The opacity of FFA is less dependent on frequency than the case for uniform absorbers, i.e., $\tau_{\text{ff}} \propto \nu^{-0.57 \pm 0.10}$. Thus, it suggests that a absorbing medium would be a highly inhomogeneous structure and it is

consistent with the previous work of [Fujita & Nagai \(2017\)](#).

- Based on the measured flux asymmetry between the counter and approaching lobes, we constrain the number density of the FFA foreground n_{CND} as $1.8 \times 10^4 \text{ cm}^{-3} \lesssim n_{\text{CND}} \lesssim 1.0 \times 10^6 \text{ cm}^{-3}$, considering the uncertainties of temperature and path length of CNDs having gradual change in the plasma density. We also discuss the case of non-uniform CNDs containing clumpy clouds. By considering the size of clouds with sub-pc, we constrain the number density of cloud with $3.0 \times 10^5 \text{ cm}^{-3} \leq \bar{n}_c \leq 4.0 \times 10^6 \text{ cm}^{-3}$. In both cases, the derived electron number density is higher than the typical value ($\bar{n}_c = 10^{2-4} \text{ cm}^{-3}$) seen in narrow-line region, suggesting that such dense ionized clumps might be located at pc-scale central region of 3C 84.

ACKNOWLEDGMENTS

We are grateful to the anonymous referee for valuable comments, which improved the manuscript. We acknowledge all staff members and students at KVN and VERA who supported the operation of the array and the correlation of the data. KVN is a facility operated by the Korea Astronomy and Space Science Institute. VERA is a facility operated by National Astronomical Observatory of Japan in collaboration with associated universities in Japan. This work is partially supported by JSPS KAKENHI Grant Numbers JP18K03656 and JP18H03721 (MK). NK acknowledges the financial support of Grant-in-Aid for Young Scientists (B:16K17670) and Grant-in-Aid for Scientific Research (C:19K03918).

REFERENCES

- Abdo, A. A., Ackermann, M., Ajello, M., et al 2009, *ApJ*, 699, 31
- Alonso-Herrero, A., Ramos Almeida, C., Esquej, P., et al. 2014, *MNRAS*, 443, 2766
- Alonso-Herrero, A., Ramos Almeida, C., Mason, R., et al. 2011, *ApJ*, 736, 82
- Antonucci, R. 1993, *ARA&A*, 31, 473
- Asmus, D., Hönig, S. F., & Gandhi, P. 2016, *ApJ*, 822, 109
- Asmus, D., Hönig, S. F., Gandhi, P., Smette, A., & Duschl, W. J. 2014, *MNRAS*, 439, 1648
- Audibert, A., Riffel, R., Sales, D. A., Pastoriza, M. G., & Ruschel-Dutra, D. 2017, *MNRAS*, 464, 2139
- Burtscher, L., Meisenheimer, K., Tristram, K. R. W., et al. 2013, *A&A*, 558, 149
- Chan, C.-H., & Krolik, J. H., 2016, *ApJ*, 825, 67
- Chan, C.-H., & Krolik, J. H., 2017, *ApJ*, 843, 58
- Davies, R. I., Maciejewski, W., Hicks, E. K. S., et al. 2014, *ApJ*, 792, 101
- Davies, R. I., Müller Sánchez, F., Genzel, R., et al. 2007, *ApJ*, 671, 1388
- Deller, A. T., Brisken, W. F., Phillips, C. J., et al. 2011, *PASP*, 123, 275
- Diamond-Stanic, A. M., & Rieke, G. H. 2012, *ApJ*, 746, 168
- Dorodnitsyn, A., Kallman, T., & Proga, D. 2016, *ApJ*, 819, 115
- Elitzur, M., & Shlosman, I. 2006, *ApJL*, 648, L101
- Esquej, P., Alonso-Herrero, A., González-Martín, O., et al. 2014, *ApJ*, 780, 86
- Fujita, Y., & Nagai, H. 2017, *MNRAS*, 465, L94
- García-Burillo, S., Combes, F., Usero, A., et al. 2014, *A&A*, 567, 125
- Gaspari, M., Ruszkowski, M., & Oh, S. P. 2013, *MNRAS*, 432, 3401

- Greisen, E. W. 2003, in *Information Handling in Astronomy — Historical Vistas*, ed. A. Heck (Dordrecht: Kluwer), 109
- Hicks, E. K. S., Davies, R. I., Maciejewski, W., et al. 2013, *ApJ*, 768, 107
- Hitomi Collaboration, Aharonian, F., Akamatsu, H., et al. 2018, *PASJ*, 70, 13
- Hiura, K., Nagai, H., Kino, M., et al. 2018, *PASJ*, 70, 83
- Hönig, S. F., & Beckert, T. 2007, *MNRAS*, 380, 1172
- Ichikawa, K., Packham, C., Ramos Almeida, C., et al. 2015, *ApJ*, 803, 57
- Imanishi, M., Ichikawa, K., Takeuchi, T., et al. 2011, *PASJ*, 63, 447
- Imanishi, M., Nakanishi, K., & Izumi, T. 2016, *ApJL*, 822, L10
- Imanishi, M., Nakanishi, K., Izumi, T., & Wada, K. 2018, *ApJL*, 853, L25
- Imanishi, M., & Wada, K. 2004, *ApJ*, 617, 214
- Izumi, T., Wada, K., Fukushige, R., Hamamura, S., & Kohno, K. 2018, *ApJ*, 867, 48
- Jaffe, W., Meisenheimer, K., Röttgering, H. J. A., et al. 2004, *Nature*, 429, 47
- Jorstad, S. G., Marscher, A. P., Morozova, D. A., et al. 2017, *ApJ*, 846, 98
- Kameno, S., Horiuchi, S., Shen, Z.-Q., et al. 2000, *PASJ*, 52, 209
- Kameno, S., Sawada-Satoh, S., Inoue, M., Shen, Z.-Q., & Wajima, K. 2001, *PASJ*, 53, 169
- Kawaguchi, T., & Mori, M. 2011, *ApJ*, 737, 105
- Kawakatu, N., & Wada, K. 2008, *ApJ*, 681, 73
- Kawakatu, N., Wada, K., & Ichikawa, K. 2020, *ApJ*, 889, 84
- Kim, J.-Y., Krichbaum, T. P., Marscher, A. P., et al. 2019, *A&A*, 622, 196
- Kino, M., Wajima, K., Kawakatu, N., et al. 2018, *ApJ*, 864, 118
- Komatsu, E., Dunkley, J., Nolte, M. R., et al. 2009, *ApJS*, 180, 330
- Krolik, J. H. 2007, *ApJ*, 661, 52
- Krolik, J. H., & Begelman, M. C. 1988, *ApJ*, 329, 702
- Lee, S.-S., Byun, D.-Y., Oh, C. S., et al. 2015b, *Journal of the Korean Astronomical Society*, 48, 229
- Lee, S.-S., Oh, C. S., Roh, D.-G., et al. 2015a, *Journal of the Korean Astronomical Society*, 48, 125
- Lee, S.-S., Wajima, K., Algaba, J.-C., et al. 2016, *ApJS*, 227, 8
- Levinson, A., Laor, A., & Vermeulen, R. C. 1995, *ApJ*, 448, 589
- López-Gonzaga, N., Burtscher, L., Tristram, K. R. W., Meisenheimer, K., & Schartmann, M. 2016, *A&A*, 591, 47
- Mallmann, N. D., Riffel, R., Storchi-Bergmann, T., et al. 2018, *MNRAS*, 478, 5491
- Markowitz, A. G., Krumpke, M., & Nikutta, R. 2014, *MNRAS*, 439, 1403
- Murayama, T., & Taniguchi, Y. 1998, *ApJL*, 497, L9
- Nagai, H., Fujita, Y., Nakamura, M., et al. 2017, *ApJ*, 849, 52
- Nagai, H., Haga, T., Giovannini, G., et al. 2014, *ApJ*, 785, 53
- Nagai, H., Onishi, K., Kawakatu, N., et al. 2019, *ApJ*, 883, 193
- Nagai, H., Orienti, M., Kino, M., et al. 2012, *MNRAS*, 423, L122
- Nagai, H., Suzuki, K., Asada, K., et al. 2010, *PASJ*, 62, L11
- Namekata, D., & Umemura, M. 2016, *MNRAS*, 460, 980
- Namekata, D., Umemura, M., & Hasegawa, K. 2014, *MNRAS*, 443, 2018
- Nomura, M., Ohsuga, K., Takahashi, H. R., Wada, K., & Yoshida, T. 2016, *PASJ*, 68, 16
- Ohsuga, K., & Umemura, M. 2001, *ApJ*, 559, 157
- Osterbrock, D. E. 1989, *Astrophysics of Gaseous Nebulae and Active Galactic Nuclei* (Mill Valley, CA: Univ. Sci. Books)
- Pearson, T. J., & Readhead, A. C. S. 1984, *ARA&A*, 22, 97
- Plambeck, R. L., Bower, G. C., Rao, R., et al. 2014, *ApJ*, 797, 66
- Ramos Almeida, C., Levenson, N. A., Alonso-Herrero, A., et al. 2011, *ApJ*, 731, 92
- Ramos Almeida, C., & Ricci, C. 2017, *NatAs*, 1, 679
- Scharwächter, J., McGregor, P. J., Dopita, M. A., & Beck, T. L. 2013, *MNRAS*, 429, 2315
- Shepherd, M. C. 1997, in *ASP Conf. Ser. 125, Astronomical Data Analysis Software and Systems VI*, ed. G. Hunt & H. E. Payne (San Francisco: ASP), 77
- Sutherland, R. S., & Dopita, M. A. 1993, *ApJS*, 88, 253
- Suzuki, K., Nagai, H., Kino, M., et al. 2012, *ApJ*, 746, 140
- Tanimoto, A., Ueda, Y., Odaka, H., et al. 2019, *ApJ*, 877, 95
- Tavecchio, F., & Ghisellini, G. 2014, *MNRAS*, 443, 1224
- Thompson, A. R., Moran, J. M., & Swenson, G. W., Jr. 2001, *Interferometry and Synthesis in Radio Astronomy*, 2nd ed. (New York: John Wiley & Sons)
- Thompson, T. A., Quataert, E., & Murray, N. 2005, *ApJ*, 630, 167
- Tristram, K. R. W., Burtscher, L., Jaffe, W., et al. 2014, *A&A*, 563, 82
- Umemura, M., Fukue, J., & Mineshige, S. 1998, *MNRAS*, 299, 1123
- Urry, C. M., & Padovani, P. 1995, *PASP*, 107, 803
- Vollmer, B., Beckert, T., & Davies, R. I. 2008, *A&A*, 491, 441
- Walker, R. C., Dhawan, V., Romney, J. D., Kellermann, K. I., & Vermeulen, R. C. 2000, *ApJ*, 530, 233
- Wada, K. 2012, *ApJ*, 758, 66
- Wada, K., & Norman, C. A. 2002, *ApJL*, 566, L21
- Wada, K., Papadopoulos, P. P., & Spaans, M. 2009, *ApJ*, 702, 63
- Wada, K., Schartmann, M., & Meijerink, R. 2016, *ApJL*, 828, L19
- Wada, K., Yonekura, K., & Nagao, T. 2018, *ApJ*, 867, 49